MNRAS **000**, 000–000 (0000) Preprint November 23, 2020 Compiled using MNRAS LATEX style file v3.0

Gravitational-wave Signals From Three-dimensional Supernova Simulations With Different Neutrino-Transport Methods

H. Andresen[1]★, R. Glas[2,3], H.-Th. Janka[2],
[1]*Max Planck Institute for Gravitational Physics (Albert Einstein Institute), Am Mühlenberg 1, Potsdam-Golm, D-14476, Germany*
[2]*Max-Planck-Institut für Astrophysik, Karl-Schwarzschild-Str. 1, D-85748 Garching, Germany*
[3]*Excellence Cluster ORIGINS, Boltzmannstr. 2, D-85748 Garching, Germany*

November 23, 2020

ABSTRACT

We compare gravitational-wave (GW) signals from eight three-dimensional simulations of core-collapse supernovae from Glas et al. (2019), using two different progenitors with zero-age main sequence masses of 9 and 20 solar masses ($M_\odot$). The collapse of each progenitor was simulated four times, at two different grid resolutions and with two different neutrino transport methods, using the Aenus-Alcar code. The main goal of this study is to assess the validity of recent concerns that the so-called "Ray-by-Ray+" (RbR+) approximation is problematic in core-collapse simulations and can adversely affect theoretical GW predictions. Therefore, signals from simulations using RbR+ are compared to signals from corresponding simulations using a fully multidimensional (FMD) transport scheme. The $9M_\odot$ progenitor successfully explodes, whereas the $20M_\odot$ model does not. Both the standing accretion shock instability and hot-bubble convection develop in the postshock layer of the non-exploding models. In the exploding models, neutrino-driven convection in the postshock flow is established around 100 ms after core bounce and lasts until the onset of shock revival. We can, therefore, judge the impact of the numerical resolution and neutrino transport under all conditions typically seen in non-rotating core-collapse simulations. We find excellent qualitative agreement in all GW features and mostly very satisfactory quantitative agreement between simulations using the different transport schemes. Overall, resolution-dependent differences in the hydrodynamic behaviour of low-resolution and high-resolution models turn out to have a greater impact on the GW signals than consequences of the different transport methods. Furthermore, increasing the resolution decreases the discrepancies between models with different neutrino transport.

Key words: gravitational waves – supernovae: general – hydrodynamics – instabilities

1 INTRODUCTION

During the last decade theoretical predictions of GWs emitted during the deaths of massive stars based on fully three-dimensional (3D) simulations (Wongwathanarat et al. 2010; Takiwaki et al. 2012; Hanke et al. 2013; Takiwaki et al. 2014; Lentz et al. 2015; Wongwathanarat et al. 2015; Müller 2015; Melson et al. 2015; Roberts et al. 2016; Müller et al. 2017; Kuroda et al. 2016a,b, 2017; Summa et al. 2018; O'Connor & Couch 2018; Ott et al. 2018; Glas et al. 2019) have been published by several authors (Müller et al. 2012; Yakunin et al. 2015; Kuroda et al. 2016b; Andresen et al. 2017; O'Connor & Couch 2018; Andresen et al. 2019; Powell & Müller 2019; Radice et al. 2019; Vartanyan et al. 2019; Powell & Müller 2020; Mezzacappa et al. 2020). For non-rotating and slowly rotating progenitors, two signal components have been found to dominate the GWs. Emission below 250 Hz (low-frequency emission) has been associated (Kuroda et al. 2016b; Andresen et al. 2017) with the so-called standing accretion shock instability (SASI) (Blondin et al. 2003) that develops in a subset of all simulations (see for example Hanke et al. 2013). Recently, Powell & Müller (2020) presented signals from a non-exploding simulation. In one of their models the GWs generated by SASI activity reached frequencies of $\sim$ 400 Hz, due to the small average shock radius at late times seen in this model. In addition to the low-frequency GWs, oscillations of the proto-neutron star (PNS) lead to emission above 300 Hz (Marek et al. 2009; Murphy et al. 2009; Müller et al. 2013). This signal component, which we will refer to as high-frequency emission, is seen in all modern simulations and exhibits a secular increase in emission frequency as time progresses.

Complementary to the theoretical efforts, the GW-astronomy community has developed methods to specifically search for and characterise supernova GW signals in both current and future laser interferometers

★ E-mail: haakon.andresen@aei.mpg.de

(Logue et al. 2012; Gossan et al. 2016; Powell et al. 2016; van Putten 2016; Powell et al. 2017; Gill et al. 2018; Astone et al. 2018; Powell 2018; Roma et al. 2019; Suvorova et al. 2019). The LIGO-Virgo collaboration has performed follow-up searches for optically observed supernovae during their first observation run (Abbott et al. 2016) and later updated their results with data from their second observation run (Abbott et al. 2020). The null observations of these searches put constraints on the energy emitted in GWs by the supernovae and, as a consequence, constrains the emission models and progenitor properties. Observational efforts are hampered by the fact that we can not construct template banks, which is the standard for compact binary mergers. This is due to the stochastic nature of the fluid dynamics, the uncertainties in the underlying physics, and the high computational cost of simulations. To improve detection prospects of supernova GWs, the core-collapse supernova modelling community must provide predictions that are as accurate as possible and for which systematic effects in the signals are well understood.

The spectral properties of the individual signal components and how they depend on the evolution of global features of the simulations are by now reasonably well understood (Sotani et al. 2017; Torres-Forné et al. 2018; Morozova et al. 2018; Torres-Forné et al. 2019a,b; Sotani & Takiwaki 2020); the prevalence, strength and validity of different signal components are still, however, debated in the literature (see the discussion in Radice et al. 2019 and Mezzacappa et al. 2020). The roots of this discussion are the uncertainties that remain in supernova modelling because the properties of the GW signals are inherently tied to the underlying model dynamics.

One possible source of model differences can be the treatment of neutrino transport and the associated neutrino-matter interactions. The energy deposited behind the shock by neutrinos radiated away from the PNS plays a crucial role in launching the supernova shock, which initially stalls at about one hundred kilometres from the centre. Furthermore, the development of hydrodynamic instabilities, the properties of the PNS, and the conditions in the postshock region are closely connected to the details of the neutrino radiation. Radiation transport schemes used in simulations today are approximate solutions of the full Boltzmann problem, which is currently not feasible to solve in 3D simulations. A method that has been extensively employed is the RbR+ neutrino-transport scheme (Rampp & Janka 2002; Buras et al. 2006; Bruenn et al. 2013), which has the advantage of being well suited for large numerical simulations. The formulation lends itself to parallelisation and scales well with the number of computation nodes. However, in the RbR+ approximation, only radial neutrino fluxes are taken into account. This has been the cause of some concerns within the core-collapse modelling community and it has been shown that the RbR+ scheme can lead to artificial results in axis-symmetric simulations (Skinner et al. 2016; Just et al. 2018; Glas et al. 2019). Naturally, this could, in turn, lead to errors in the GWs predictions. However, due to the inverse cascade of energy and strict symmetry constraints imposed in two spatial dimensions, it is not clear that results from axis-symmetric simulations can be extrapolated to full 3D simulations. Indeed, Glas et al. (2019) compared multidimensional simulations with the RbR+ and FMD schemes and found excellent agreement in the overall evolution of the fluid flow in the 3D simulations. The RbR+ transport scheme leads to more pronounced local and instantaneous variations in the neutrino heating/cooling rates and neutrino fluxes, but in 3D such regions are short lived and do not grow to larger-scale, more coherent, flow patterns.

In this work, we will present the GW signals from the eight 3D core-collapse supernova simulations of Glas et al. (2019). The model set contains two different progenitors, simulated at two grid resolutions with the RbR+ and FMD transport schemes. Our primary goal is to investigate the differences between GWs from simulations using the RbR+ scheme and simulations that were conducted with FMD transport. We will perform a detailed analysis of the signals to determine if any differences between the signals go beyond the stochastic nature of core-collapse simulations. We will also study how the GWs depend on the numerical resolution and compare resolution effects to differences induced by changing the neutrino transport scheme.

In section 2 we will describe how the GWs are extracted from the simulations, summarise current results based on 3D simulations, and show how the global properties of the model dynamics relate to the typical features of the GW signals. The numerical methods are described in section 3. The model dynamics and GW signals of the best-resolved models are presented in section 4, and the discrepancies and similarities of the signals from different simulations will also be discussed in this section. The results from the low-resolution simulations are presented in section 5. We will give a summary of our main findings and our conclusions in section 6.

2 GRAVITATIONAL WAVES FROM CORE-COLLAPSE SUPERNOVAE

In this section, we first give a brief description of how we extract the signals from the simulation output. We will then summarise current core-collapse GW theory, focusing on how the spectral properties of the signals are connected to the global model properties. These results have been established in the literature over the last few years and we will only give an overview together with the appropriate references.

2.1 Extracting the Gravitational Waves

The GW signals are extracted from the hydrodynamic simulations by post-processing the output data using the quadrupole formula. In the transverse-traceless (TT) gauge the GW tensor can be expressed in terms of two independent components, h_+ and $h_\times$. Far away from the source, at a distance D, and in the slow-motion limit, the two components can be expressed in the spherical coordinate system of the simulations as follows:

$$\begin{aligned} h_+ = \frac{G}{c^4 D}\Big[&\ddot{Q}_{11}(\cos^2\phi - \sin^2\phi\cos^2\theta) \\ &+ \ddot{Q}_{22}(\sin^2\phi - \cos^2\phi\cos^2\theta) - \ddot{Q}_{33}\sin^2\theta \\ &- \ddot{Q}_{12}(1+\cos^2\theta) + \ddot{Q}_{13}\sin\phi\sin 2\theta \\ &+ \ddot{Q}_{23}\cos\phi\sin 2\theta\Big] \end{aligned} \tag{1}$$

and

$$\begin{aligned} h_\times = \frac{G}{c^4 D}\Big[&(\ddot{Q}_{11} - \ddot{Q}_{22})\sin 2\phi\cos\theta \\ &+ \ddot{Q}_{12}\cos\theta\cos 2\phi - \ddot{Q}_{13}\cos\phi\sin\theta\Big]. \end{aligned} \tag{2}$$

Here θ represents the polar angle, and ϕ is the azimuthal angle of the spherical coordinate system defined by the simulation grid. We use c for the speed of light and G is Newton's constant. $\ddot{Q}_{ij}$ denotes the second-order time derivatives of the Cartesian components of the quadrupole moment (with $i, j = 1, 2, 3$), and is given by

$$\ddot{Q}_{ij} = \mathrm{STF}\left[2\int d^3x\,\rho\left(v_i v_j - x_i\partial_j\Phi\right)\right]. \tag{3}$$

In this form, the time derivatives of the original definition have been eliminated to avoid numerical problems associated with second-order derivatives (Oohara et al. 1997; Finn 1989; Blanchet et al. 1990). In Eq. (3), v_i are the Cartesian velocity components, x_i the Cartesian coordinates, the gravitational potential is represented by Φ (including post-Newtonian corrections used in the simulations), and ρ is the local fluid density. STF denotes the symmetric trace-free projection operator. In the following, we do not give the GW strain h_+ and $h_\times$, but the *GW amplitudes:*

$$A_+ \equiv Dh_+, \qquad A_\times \equiv Dh_\times. \tag{4}$$

For a more detailed derivation of the above equations see Müller et al. (2012) and Andresen et al. (2017).

We compute spectrograms by applying short-time Fourier transforms (STFT) to A_+ and $A_\times$ individually, and we square the output before adding them together. Before plotting, we normalise the STFT and take the logarithm. The normalisation is such that the logarithmic value lies in the range of $(-\infty, 0]$. The same factor is applied for each model so that the plots can be directly compared. In other words, we define and plot

$$\Pi(A_+, A_\times) \equiv \log_{10} \gamma[\mathrm{STFT}(A_+)^2 + \mathrm{STFT}(A_\times)^2], \tag{5}$$

where γ is the normalisation factor. We use $\gamma = 1/0.05$. For a discrete signal, the STFT is obtained by applying a discrete Fourier transform (DFT) to the signal with a sliding window. We use the following DFT definition:

$$\widetilde{X}_k(f_k) = \frac{1}{M} \sum_{m=1}^{M} x_m e^{-2\pi i k m/M}. \tag{6}$$

Here, x_m is the discrete time-domain signal, consisting of M samples. $f_k = k/T$ represents the frequency of bin k, where T is the signal length. The spectrograms shown in this work use a window length of 60 ms. The signal segments are convolved with a Blackman window before the DFT is applied, and we filter out anything above 1200 Hz or below 25 Hz in the DFTs.

The total energy, E, radiated in GWs by a source is given by

$$E = \frac{G}{5c^5} \int \mathrm{d}t \, \dddot{Q}_{ij} \dddot{Q}_{ij}. \tag{7}$$

Here $\dddot{Q}_{ij}$ are the third-order time derivatives of the quadrupole moment components. The corresponding spectral energy density of the GWs, for a discrete time signal with duration T, is

$$\left[\frac{\Delta E}{\Delta f}\right]_k = \frac{2G}{5c^5} (2\pi f_k)^2 \left[\left|\widetilde{\dddot{Q}}_{ij} \widetilde{\dddot{Q}}_{ij}\right|\right]_k T^2. \tag{8}$$

The simulations we study in this work were terminated at different times, and the GW emission had not subsided when the simulations ended. The dependency on the signal length in Eq. (8) is, therefore, disadvantageous for our comparison of the different GW signals. We circumvent this problem by calculating the spectral energy density for a time window determined by the duration of the shortest signal of each model set. For the s9 models, we calculate the spectral energy density of the GWs emitted between 50 and 420 ms post bounce, and for the s20 models the time window stretches from 50 to 570 ms post bounce.

2.2 The Characteristics of Gravitational Waves from Three-dimensional Simulations

By now, the typical GWs emitted during the core collapse of slowly rotating (and non-rotating) progenitors have been well established in the literature (Marek et al. 2009; Murphy et al. 2009; Müller et al. 2012, 2013; Yakunin et al. 2015; Kuroda et al. 2016b; Sotani et al. 2017; Andresen et al. 2017; Torres-Forné et al. 2018; Morozova et al. 2018; O'Connor & Couch 2018; Andresen et al. 2019; Powell & Müller 2019; Radice et al. 2019; Torres-Forné et al. 2019a,b; Vartanyan et al. 2019; Sotani & Takiwaki 2020; Mezzacappa et al. 2020). The signal predictions are diverse and several unique signal components have been discovered, but two of these are most prevalent in recent GW predictions. Emission with an almost linear increase in frequency as a function of time is found above 300 Hz. It was first seen in two-dimensional simulations and was suggested to be associated with buoyancy processes in the surface of the PNS (Marek et al. 2009; Murphy et al. 2009; Müller et al. 2013). It was shown that the central frequency of this emission component closely traces the Brunt-Väisäla frequency in the PNS surface region (Murphy et al. 2009; Müller et al. 2013), which was also found to be the case for signals from recent 3D simulations (Andresen et al. 2017; Morozova et al. 2018; Andresen et al. 2019; O'Connor & Couch 2018).

The Brunt-Väisäla frequency (N) is given in terms of the sound speed (c_s), the pressure (P), the gravitational potential (Φ), and the density (ρ) as follows:

$$N^2 = \frac{1}{\rho} \frac{\partial \Phi}{\partial r} \left[\frac{1}{c_s^2} \frac{\partial P}{\partial r} - \frac{\partial \rho}{\partial r} \right]. \tag{9}$$

Here r denotes the radial coordinate of a spherical coordinate system. The quantities in Eq. (9) are not constant over the outer PNS layer, the radial variance of these quantities as well as local perturbations cause the GW emission to spread out around the average value of N. While spatially averaging Eq. (9) over the PNS surface layer results in a good match between the average N-value and the peak-frequency measured from the spectrograms, it is not straight forward to directly discern the PNS properties based on Eq. (9). Müller et al. (2013) derived an approximation for N which facilitates a better understanding of the connection between the global PNS properties and the typical frequency ($f_{\mathrm{GW}}^{\mathrm{b}}$, here "b" denotes buoyancy) of the GWs emitted by buoyancy processes. According to Müller et al. (2013),

$$f_{\mathrm{GW}}^{\mathrm{b}} = \frac{1}{2\pi} \frac{GM_{\mathrm{PNS}}}{R_{\mathrm{PNS}}^2} \sqrt{1.1 \frac{m_n}{\langle \varepsilon_{\bar{\nu}} \rangle}} \left[1 - \frac{GM_{\mathrm{PNS}}}{R_{\mathrm{PNS}} c^2} \right]^2. \tag{10}$$

This formulation is not only informative with regard to extracting the physical parameters of the system from the signal, but it also provides some insights relevant for the purpose of this work. M_{PNS} and R_{PNS} in Eq. (10) represent the radius and mass of the PNS. The average anti-electron neutrino energy is denoted by $\langle \varepsilon_{\bar{\nu}} \rangle$, which is simply a proxy for the temperature of the PNS, and m_n is the neutron mass. If the global properties of the PNS do not depend strongly on the neutrino transport scheme, then there will be no reason to expect a large difference in the average properties of the GW emission above 300 Hz.

The second signal component commonly found is associated with the SASI. Strong emission centered around $\sim$ 75-100 Hz is found in simulations where the SASI dominates the postshock flow (Kuroda et al. 2016b; Andresen et al. 2017, 2019; O'Connor & Couch 2018). The SASI arises when perturbations created at the shock are advected with the fluid down to the PNS. These perturbations are converted to sound waves at the PNS surface which propagate back up to the shock and give rise to new perturbations. Under the right conditions this cycle grows in amplitude and results in large-scale quasi-periodic oscillations of the shock (Blondin et al. 2003; Blondin & Mezzacappa 2006; Foglizzo et al. 2007;

Ohnishi et al. 2006, 2008; Scheck et al. 2008; Guilet & Foglizzo 2012; Foglizzo et al. 2015). The typical time scale, τ, of the SASI is given by the time it takes a perturbation to be advected from the shock-front plus the time needed for the sound waves to propagate back upstream to the shock. Assuming spherical symmetry, we can estimate τ as follows:

$$\tau \approx \left[\int_{R_{\rm PNS}}^{R_{\rm S}} dr \left(\frac{1}{c_s} + \frac{1}{|v_r|} \right) \right]. \tag{11}$$

In the above expression $R_{\rm S}$ represents the average shock radius, and v_r is the advection velocity at a distance r from the origin. We can neglect the term $1/c_s$ since the sound speed in the postshock region is much larger than the advection velocity, which to first order is a linear function of the radial position, $v_r = v_{\rm PS} r / R_{\rm S}$. Here $v_{\rm PS} = -\beta^{-1} \sqrt{G M_{\rm PNS}/R_{\rm S}}$ is the postshock velocity (Müller & Janka 2014). The dimensionless parameter β is the ratio of the postshock and preshock density. The inverse of the typical SASI time scale, with a factor of two accounting for frequency doubling, sets the characteristic frequency ($f_{\rm SASI}^{\rm GW}$) of GWs associated with SASI activity. After solving the integral and inverting the expression, one finds

$$f_{\rm SASI}^{\rm GW} \approx 2\beta^{-1} \sqrt{\frac{G M_{\rm PNS}}{R_{\rm S}^3}} \left[\ln \left(R_{\rm S}/R_{\rm PNS} \right) \right]^{-1}. \tag{12}$$

For a more detailed discussion of the SASI and the typical time scale on which the instability develops and operates we refer the reader to Foglizzo et al. (2007), Scheck et al. (2008), Müller & Janka (2014), and Janka (2017). Again we see that the typical frequency depends on the properties of the PNS, but also the average shock radius. Typically, the shock trajectory exhibits a larger degree of variation between different simulations than the PNS does. Assuming that the PNS radius is 30 km and that the average shock radius is 100 km, a 10 per cent increase in the average shock radius would correspond to a $\sim$ 24 per cent decrease in $f_{\rm SASI}^{\rm GW}$. A 5 per cent larger shock radius results in roughly a 10 per cent lower emission frequency. Since the low-frequency emission is spread out in a roughly 200 Hz broad frequency range, differences in the trajectory of the shock caused by changing the neutrino-transport scheme must be systematic and sustained over long periods to have a noticeable effect of the GW signal.

3 NUMERICAL METHODS

The core-collapse simulations which this paper is based on were presented in Glas et al. (2019), they were performed with the Aenus-Alcar code (Obergaulinger 2008; Just et al. 2015, 2018). The module Aenus (Obergaulinger 2008; Just et al. 2015, 2018) uses a Godunov-type method to solve the hydrodynamical equations. The solver is a directionally unsplit finite-volume scheme in spherical coordinates (r, θ, ϕ). The high-density equation of state used was SFHo (Steiner et al. 2013), which was extended to be applicable for temperatures down to 10^{-3} MeV (Glas et al. 2019). Aenus describes self-gravity in terms of a one-dimensional potential, which includes relativistic corrections to the Newtonian potential (case A of Marek et al. 2006).

Alcar is a fully multidimensional neutrino-radiation solver that employs a two-moment scheme to evolve the two lowest angular moments of the Boltzmann equation (Just et al. 2018). Three neutrino species (electron neutrinos, electron antineutrinos, and a third species representing the remaining neutrino flavours), in 15 energy bins logarithmically spaced up to 400 MeV, were evolved in the simulations of Glas et al. (2019). The RbR+ simulations were performed by setting non-radial flux terms to zero for the duration of the simulations.

The simulations were performed with two different grid resolutions, which allowed the authors to judge the impact of numerical resolution. The two resolutions used were $(n_r,\ n_\theta,\ n_\phi) = (320,\ 40,\ 80)$ and $(n_r,\ n_\theta,\ n_\phi) = (640,\ 80,\ 160)$, here n_r, n_θ, and n_ϕ indicate the number of grid points in the radial, polar, and azimuthal directions, respectively. We will refer to the former set-up as the low-resolution simulations and use the label "L" (for low) and the latter set-up will be labelled with "H" (for high) and will be referred to as the high-resolution simulations. Note that the grids were not uniform: at the poles the last two step-sizes in the θ-direction were increased. In the high-resolution case, the step-size first increases to 4 degrees and then to 10 degrees, while for the low-resolution case the increase is first to 6 degrees and then to 12 degrees. The rest of the computational domain was covered by equally sized cells in θ.

The inner ten kilometres of the grid were evolved in spherical symmetry. This simplification is bound to have impacted the convective region within the PNS and the GWs produced there. However, since the extent of the spherical core was kept the same in every simulation and since PNS convection is not our primary focus, the relatively large spherical core should not affect the conclusion of this work. Glas et al. (2019) simulated the core collapse and the post-bounce phase of two stellar progenitors. The more massive of the two, a star with a zero-age main-sequence mass of 20 $M_\odot$ and with solar metallicity, fails to explode in the simulated period of evolution. This progenitor is described in Woosley & Heger (2007). The simulations based on the second star, which is a solar metallicity star with a zero-age main-sequence mass of 9 $M_\odot$, results in successful explosions. The progenitor is a modified version (Sukhbold et al. 2016) of one of the progenitors described in Woosley & Heger (2015).

4 HIGH-RESOLUTION SIMULATIONS

Since the high-resolution simulations are the most interesting for this work, we will focus on them here and return to the low-resolution simulations towards the end of this paper. Separating the resolution aspect avoids confusing the model description and the following discussion, the reader can find a detailed and in-depth description of all the simulations in Glas et al. (2019). In the following sections, we adopt a naming convention where a progenitor name (s9 or s20) followed by either "-RbR" or "-FMD" indicates the model simulated with the RbR+ or FMD neutrino transport scheme, respectively. We remind the reader that a -H is appended to the model names of the high-resolution models and that a model name ending in -L indicates a low-resolution model.

Our discussion of the model dynamics will focus mainly on the aspects directly relevant to the GW signals.

4.1 Model Dynamics

Changing the neutrino treatment in the high-resolution simulations does not lead to large differences in the model dynamics. The average shock radius, the PNS radius, the neutrino heating rate, and the prevalence of hydrodynamic instabilities are remarkably similar between the different realisations of the post-bounce phase of both s9 and s20. However, spatial and temporal variations in the details do occur. In both high-resolution simulations of the s20 progenitor, the shock front follows roughly the same trajectory, see

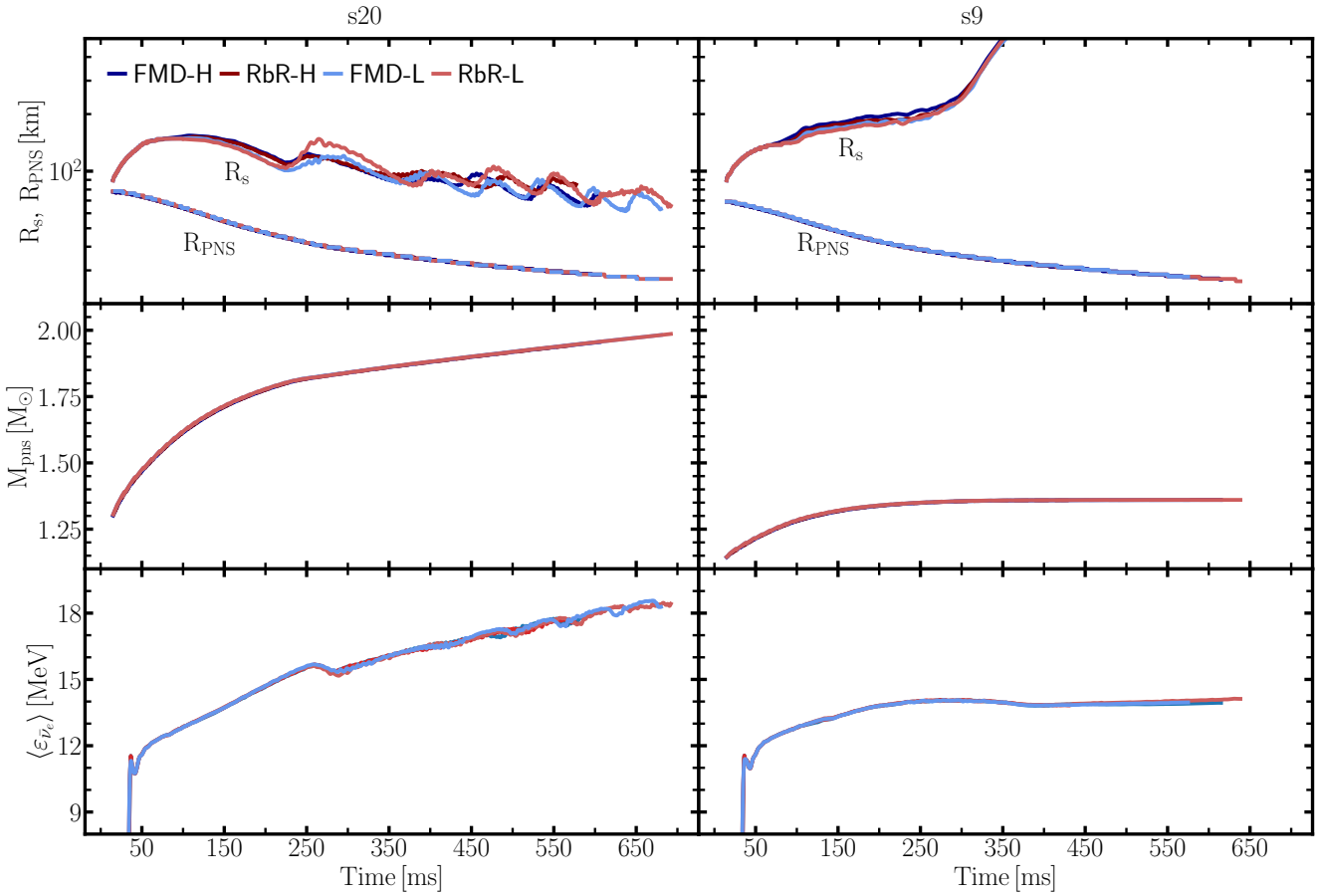

Figure 1. Average shock radius (R_s), PNS radius (R_{PNS}), PNS mass (M_{PNS}), and the average electron antineutrino energy ($\langle \varepsilon_{\bar{\nu}_e} \rangle$) as a function of time. The average shock radius and the PNS radius are shown in the top panels, the middle panels show the PNS mass, and the bottom panels show the average electron antineutrino energy extracted at a radius of 400 km in the co-moving frame. The left column represents the s20 models and the right column the s9 models. Time is given in ms after core bounce.

the top left panel of Fig. 1. The initial expansion and subsequent stagnation of the shock front are followed by a period of shock contraction, starting at around 100 ms post bounce and lasting until the silicon/oxygen interface reaches the shock. As this interface passes through the shock, approximately 200 ms after core bounce, a rapid decrease in the density ahead of the shock leads to a second period of shock expansion which lasts roughly 50 ms. From around 250 ms after bounce, the shock gradually contracts until the end of the simulation. There are transient periods of expansion, but they are immediately followed by shock contraction. The conditions in the postshock layer are best described as a non-linear combination of SASI and neutrino-driven convection; the two instabilities operate concurrently with varying strength. The SASI tends to push the shock further out, which create more favourable conditions for convection. The shock starts to retreat as the SASI gives way to convection. The contraction of the shock reduces the advection time scale, which leads to the reappearance of the SASI. These processes repeat cyclically and oscillations in the average shock radius depend on the details of these highly complicated cycles. Alternating periods of shock expansion and contraction are seen in both s20-FMD-H and s20-RbR-H, but the cycles do not entirely coincide in the two models.

Models s9-RbR-H and s9-FMD-H result in successful supernova explosions. Shock revival starts ~300 ms after core bounce, see the right top panel of Fig. 1. Before this time, the average shock radius steadily increases until the conditions for runaway shock expansion are met. The s9 progenitor is characterised by a region of low density immediately around the degenerate core, which leads to low accretion rates in the two simulations. This favours the growth of convective activity and disfavors the SASI, due to the resulting large advection time scales. While strong SASI does not develop in models s9-RbR-H and s9-FMD-H, Glas et al. (2019) reported that large-scale convective plumes in the postshock layer lead to dipole deformation of the shock front. These deformations can first be seen around 100 ms after bounce, and they reach their peak between 250 and 300 ms post bounce, see the bottom panel of Fig. 13 in Glas et al. (2019). After the onset of runaway shock expansion, the accretion rate onto the PNS is further reduced. As in the case of the s20 models, the global properties of models s9-FMD-H and s9-RbR-H agree very well.

The properties of the PNS are virtually unaffected when changing the neutrino-transport scheme, and this is true for both progenitors. The radius and mass of the PNS, which are important for determining the properties of GWs, are unchanged between the FMD and RbR+ runs, see Fig. 1. Additionally, the luminosities and average energies of the emitted neutrinos show little variation between the runs with different neutrino-transport schemes. From around 400 ms after bounce, the luminosities and energies of the electron neutrinos and antineutrinos undergo variations of ~ 10-20%. The bottom panels of Fig. 1 show the average energies of

electron antineutrinos extracted at a radius of 400 km, for all four high-resolution simulations. We do not show luminosity plots since they are not directly relevant for the discussion about GW characteristics, they are shown in Fig. 7 and Fig. 14 of Glas et al. (2019). The temporal variations in the average properties of the neutrinos, seen in models s20-FMD-H and s20-RbR-H, are caused by the alternating periods of SASI and convection in the postshock layer and the resulting variations in the conditions near the PNS surface, see Glas et al. (2019).

4.2 Gravitational Waves from the High-resolution Simulations

The signals are in general very similar to what has recently been reported in the literature (see for example Kuroda et al. (2016b); Andresen et al. (2017, 2019); O'Connor & Couch (2018); Powell & Müller (2019, 2020); Mezzacappa et al. (2020)). In all the models, the typical GW amplitudes are on the order of a few centimetres, see Fig. 2 and Fig. 4. Since vigorous SASI activity does not develop in the simulations of the less massive progenitor, the signals from s9-RbR-H and s9-FMD-H consist mainly of emission above 300 Hz (Fig. 3). However, s9-RbR-H and s9-FMD-H weakly emit low-frequency GWs. The emission in the s9 models continues after shock revival, but the amplitudes are reduced by roughly a factor of two. This reduction of GW emission supports the findings of Radice et al. (2019), who found that GWs are mainly excited in the PNS surface region by turbulent downflows from the postshock layer. Andresen et al. (2017) and Andresen et al. (2019), on the other hand, reported that overshooting of convective plumes into the PNS surface layer from the convectively unstable layer below was the primary source of GW emission from the PNS.

Violent SASI activity develops in models s20-FMD-H and s20-RbR-H, which is reflected in the GW signals by emission below 250 Hz (Fig. 5). Since the postshock flow alternates between being SASI and convectively dominated, the emission associated with SASI activity is intermittent and relatively weak when, for example, compared to model m15fr of Andresen et al. (2019). The spotty emission below 250 Hz is clearly visible in all the panels of Fig. 5. Model s20-RbR-H has a period of sustained and strong low-frequency emission between 100 and 200 ms after core bounce (bottom left panel of Fig. 5) which is weaker in model s20-FMD-H. The reduction of this emission in the FMD model is partly due to the viewing angles we have chosen. A similar, but still somewhat weaker, signal component emerges in model s20-FMD-H when changing the viewing angle.

In Fig. 6 we show the time-integrated spectral energy density of the GW emission. The time integration was done over intervals determined by the duration of the shortest simulation for each of the investigated progenitors, see section 2.1. The emission from model s20-FMD-H is dominated by three broad peaks, at $\sim$ 750 Hz, 850 Hz, and 1150 Hz. Inspecting the spectrograms (Fig. 5) reveals that the peaks at 850 Hz and 1150 Hz correspond to the same physical event, a burst of emission can be seen at approximately 450 ms post bounce. The emission at 850 Hz should be emitted at 1150 Hz, but aliasing causes part of the emission to be reflected down to lower frequencies. The emission peak at 750 Hz can also be traced back to one single emission period, taking place around 550 ms post bounce. The emission of model s20-RbR-H is spread out across a range of frequencies from around 300-1000 Hz. Several narrow peaks with amplitudes $\sim$ 2 times greater than the surrounding emission pierce the relative flat spectrum of the RbR+ model (Fig. 6). These peaks represent short bursts of emission at fixed frequencies and such spikes have been associated with individual downflows impinging on the PNS surface (Marek et al. 2009; Murphy et al. 2009; Müller et al. 2013). We do not find direct counterparts to each of these peaks in the spectrograms. However, the spectrograms are only shown for two distinct observer directions and it is not surprising that not every observer can see every emission feature. The larger spectral energy density of model s20-RbR-H, compared to s20-FMD-H, is reflected in the total emitted energy (Fig. 7). Model s20-RbR-H emitted about 30 per cent more energy during the simulated time than s20-FMD-H did in the same period. At intermediate frequencies, between the two main emission bands, we witness more emission in model s20-RbR-H than in s20-FMD-H, which is also visible in Fig. 5.

The GW emission of s9-FMD-H is $\sim$ 25 per cent more energetic than the GW emission from s9-RbR-H. In the bottom panels of Fig. 6, we see that model s9-FMD-H undergoes several short bursts of GW emission and that the FMD model emits more GWs at frequencies above 900 Hz than model s9-RbR-H. Furthermore, large peaks and narrow peaks can be seen in model s9-FMD-H, which are not present in s9-RbR-H.

The central frequencies of both emission components are remarkably similar between runs with different neutrino treatments. In Fig. 8 we plot the peak frequencies of the two emission components as functions of time, which were extracted from the spectrograms by finding the maxima of the Fourier transforms in any given time window. The results for s20, shown in the left panel, include two lines for each model. The lines around 100 Hz represent the signal associated with SASI activity and the lines in the upper half of the panel represent the emission coming from PNS oscillations. In the right panel, there are no lines around 100 Hz, since the SASI does not develop in models s9-FMD-H and s9-RbR-H. We see that the emission above 300 Hz is essentially independent of the neutrino-transport scheme, the initial value and temporal evolution of the curves agree very well. The central frequency of the emission associated with the SASI also agrees well in models s20-RbR-H and s20-FMD-H.

4.3 Differences Induced by the Ray-by-Ray+ Transport Scheme

It is difficult to disentangle the fluid motions responsible for individual parts of the GW emission from the rest of the flow and trace them throughout the simulation. Consequently, we can not explain all the small variations in the GW emission of the different models. In some cases, it is not straightforward to establish whether or not differences in the signals are caused by stochastic variations or real differences induced by changing the neutrino-transport scheme. As a consequence, some of the explanations offered in this section are likely scenarios instead of proven theories. When more simulations with a wider range of resolutions and with different input physics become available, some revisions might be in order.

There is no evidence that the choice of neutrino transport scheme leads to large systematic differences in the GW emission. The signals from simulations with different neutrino transport have similar amplitudes. Furthermore, we found no consistent trends in the spectral properties of the signals in correlation with the applied neutrino transport scheme. The RbR simulations of the s20 progenitor are more energetic and emit more GWs at higher frequencies than their FMD counterparts, but for the s9 progenitor the situation is reversed. Model s20-RbR-H emits more GWs between the two main emission bands than model s20-FMD-H, but the difference is small and emission at intermittent frequencies can not be seen

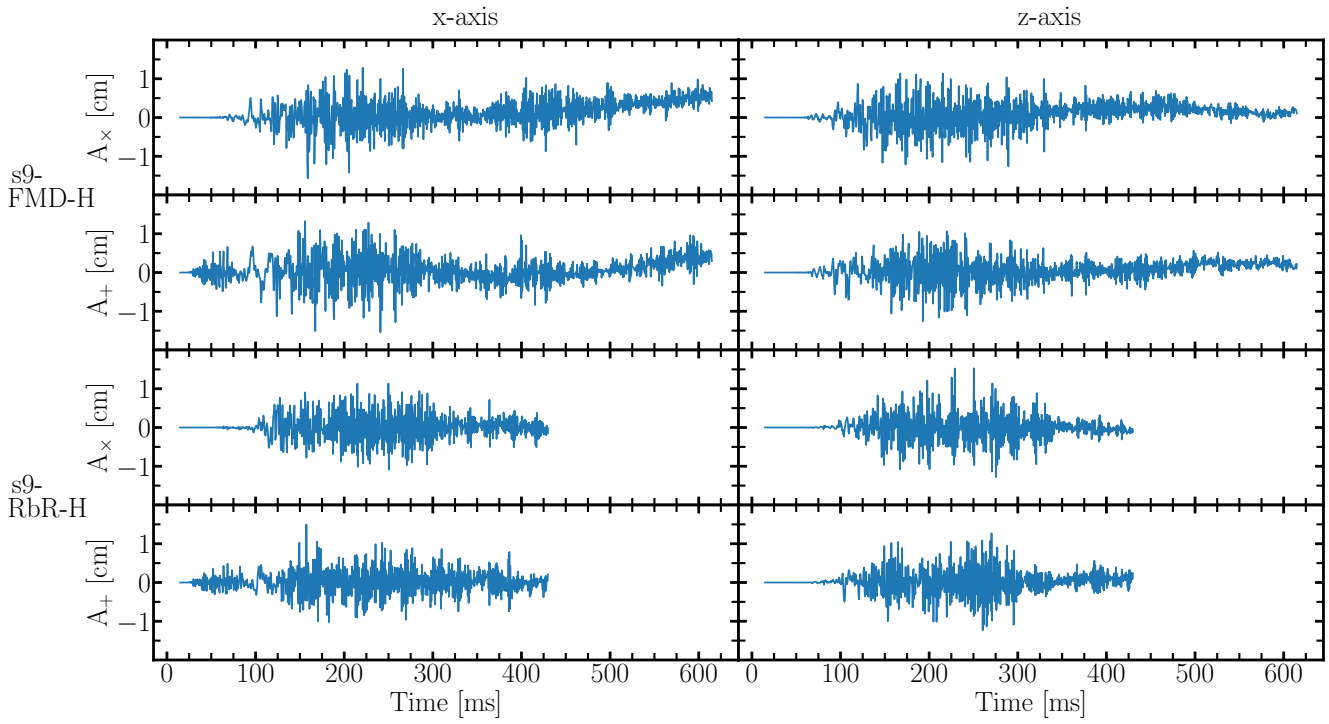

Figure 2. GW amplitudes A_+ and $A_\times$ as functions of time after core bounce for models s9-FMD-H (top two rows) and s9-RbR-H (bottom two rows). The two columns show the amplitudes for two observers, one along the z-axis (right) and one along the x-axis (left).

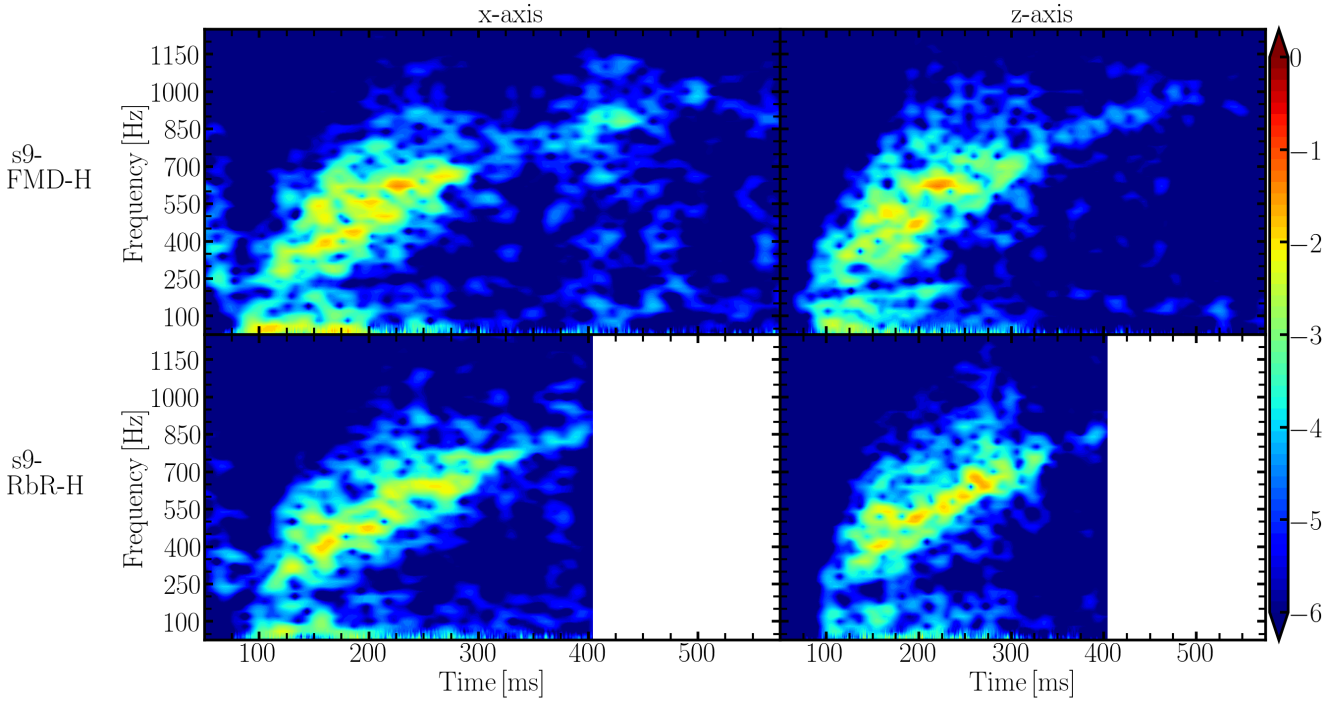

Figure 3. Spectrograms, as defined by Eq. (5), for models s9-FMD-H (top row) and s9-RbR-H (bottom row). Time is given in ms after core bounce. The two columns show the amplitudes for two observers, one along the z-axis (right) and one along the x-axis (left). The colour scale is logarithmic.

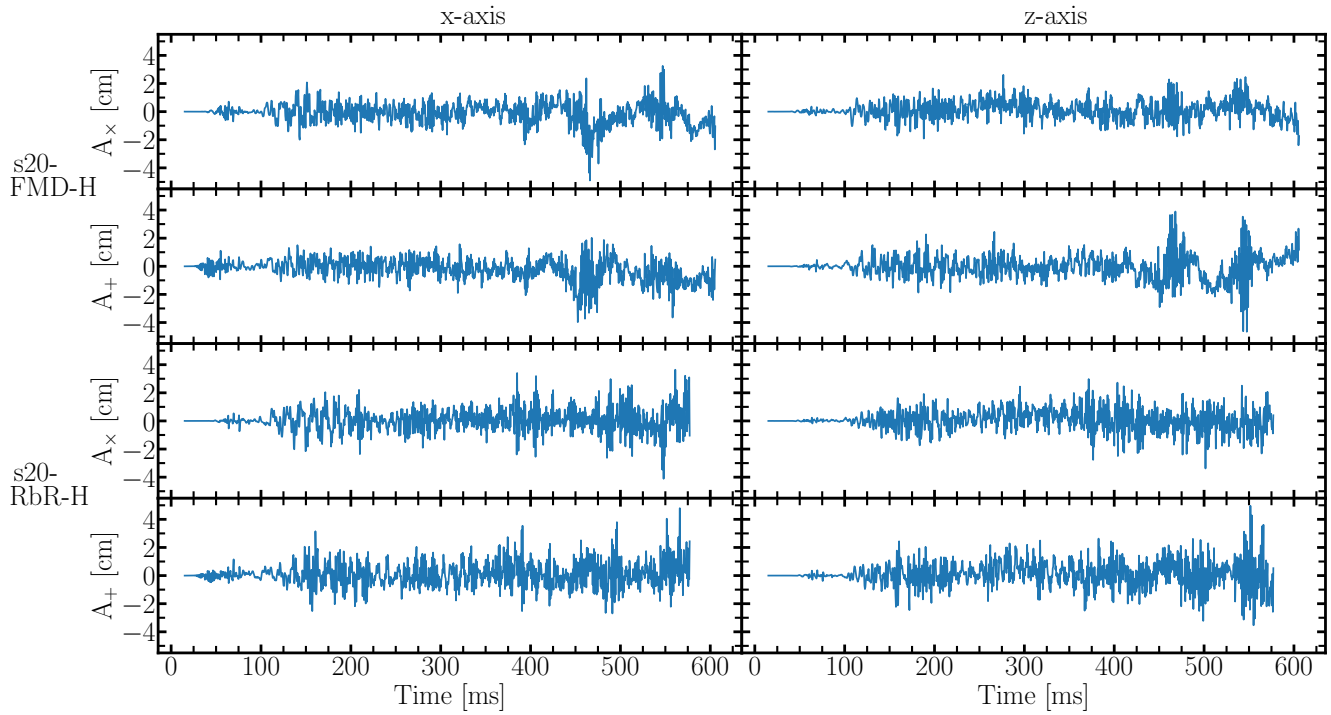

Figure 4. GW amplitudes A_+ and $A_\times$ as functions of time after core bounce for models s20-FMD-H (top two rows) and s20-RbR-H (bottom two rows). The two columns show the amplitudes for two observers, one along the z-axis (right) and one along the x-axis (left).

in the s9 models. The typical emission frequencies agree well in all models and this can easily be understood from Eq. (10) and Eq. (12) in conjuncture with Fig. 1. The global properties of the simulations that set the typical emission frequencies, the average shock radius, and the mass, temperature (or the average electron antineutrino energy), and radius of the PNS do not significantly differ between the RbR+ and FMD models. We do, therefore, not see substantial differences in the typical properties of the signals from the models with different neutrino transport, at least not systematic ones that occur in all cases as a clear consequence of the employed transport method.

The strong low-frequency emission that an observer situated in the equatorial plane (of the simulation grid) would observe between 100 and 250 ms post bounce in model s20-RbR-H (see Fig. 5) raises several questions. It is not apparent why the emission is so strong, why it appears in a very narrow frequency range, and why it is not seen with equal strength in model s20-FMD-H (though stronger than visible in Fig. 5 for other observer directions). Strong and coherent emission at low-frequencies, similar to what we see in models s20-FMD-H and s20-RbR-H, has been connected to vigorous SASI activity in the postshock layer (Kuroda et al. 2016b; Andresen et al. 2017, 2019; O'Connor & Couch 2018; Powell & Müller 2019, 2020). Strong SASI activity is often associated with sizable and coherent dipolar deformation of the stalled shock front, see for example Hanke et al. (2013). In both s20-FMD-H and s20-RbR-H, the dipole deformation of the shock front is constrained to $\sim$ 1 per cent of the average shock radius during the first 200 ms post bounce (see Fig. 6 of Glas et al. (2019)). The fluid flow appears to be convectively dominated in both models, as suggested by the $\chi > 3$ parameter criterion, which, however, is not rigorously accurate in a quantitative manner. However, a quadrupole pattern is present in the flow of both s20-FMD-H and s20-RbR-H, which is evident when considering the energy spectrum of non-radial turbulent mass motions ($E_{\rm turb}(\ell)$) in the postshock layer. We define $E_{\rm turb}(\ell)$ as follows:

$$E_{\rm turb}(\ell) = \frac{1}{V}\int_{R_{\rm PNS}}^{R_{\rm s}} r^2 {\rm d}r \sum_{m=-\ell}^{\ell} \left| \int {\rm d}\Omega Y_\ell^m \sqrt{\rho(v_\phi^2 + v_\theta^2)} \right|^2, \quad (13)$$

where v_ϕ is the fluid velocity in the azimuthal direction, v_θ is the fluid velocity in the polar direction, and V is the total volume of the postshock layer

$$V = \frac{4}{3}\pi(R_{\rm s}^3 - R_{\rm PNS}^3). \quad (14)$$

Note that we define the integration limits in the radial direction by the average shock radius and the PNS surface (defined to be where the angle-averaged density drops below 10^{11} g/cm^3). In Eq. (13), Y_ℓ^m represents the spherical harmonic functions expressed in their real form,

$$Y_\ell^m = \begin{cases} N_\ell^{|m|} P_\ell^{|m|}(\cos\theta)\sin(|m|\phi) & \text{if } m < 0, \\ N_\ell^0 P_\ell^0(\cos\theta) & \text{if } m = 0, \\ N_\ell^m P_\ell^m(\cos\theta)\cos(m\phi) & \text{if } m > 0. \end{cases} \quad (15)$$

Here ℓ and m are the degree and order, respectively, of the spherical harmonic functions and N_ℓ^m is given by

$$N_\ell^m = (-1)^m \sqrt{2}\sqrt{\frac{2\ell+1}{4\pi}\frac{(\ell-|m|)!}{(\ell+|m|)!}}, \quad (16)$$

and P_ℓ^m is the associated Legendre polynomial of degree ℓ and order m. The stochastic nature of turbulence causes temporal fluctuations in the turbulent energy spectrum and we, therefore, show the time-averaged spectrum,

$$\langle E_{\rm turb}(\ell)\rangle = \frac{1}{t_1 - t_0}\int_{t_0}^{t_1} E_{\rm turb}(\ell){\rm d}t, \quad (17)$$

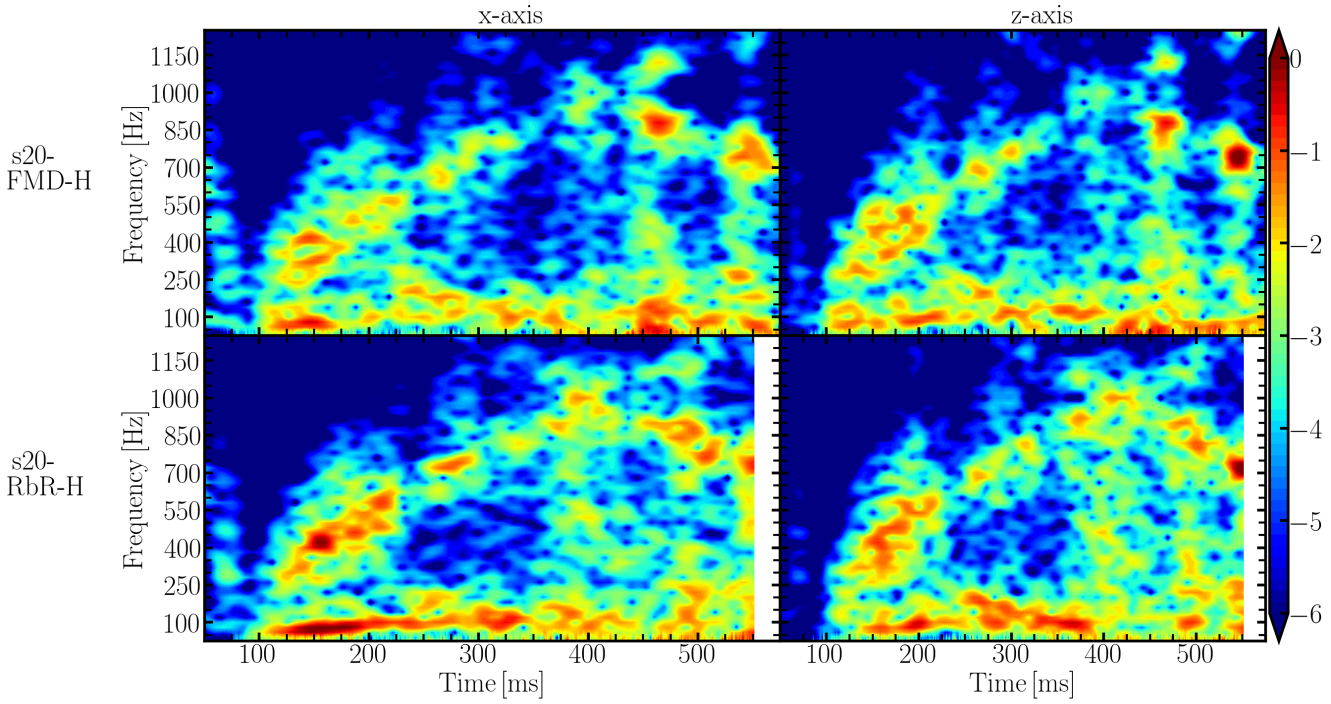

Figure 5. Spectrograms, as defined by Eq. (5), for models s20-FMD-H (top row) and s20-RbR-H (bottom row). Time is given in ms after core bounce. The two columns show the amplitudes for two observers, one along the z-axis (right) and one along the x-axis (left). The colour scale is logarithmic.

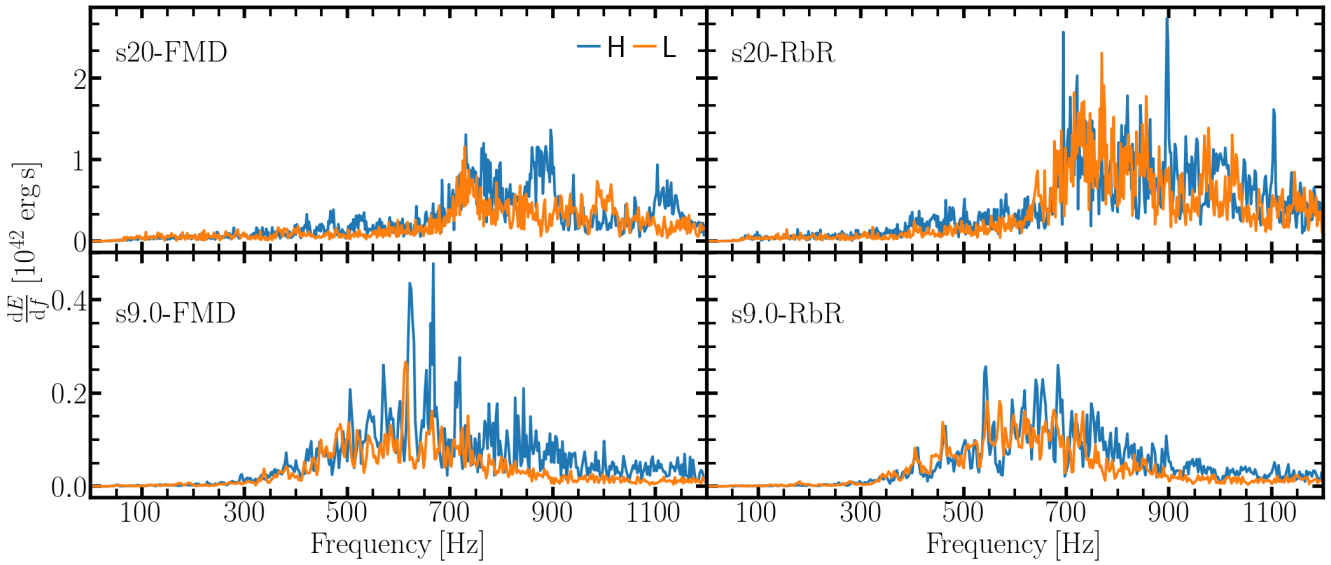

Figure 6. Total time-integrated spectral energy density (Eq. (8)) of the GWs for all eight models. The top row shows results for the s20 simulations, which were obtained from the emission between 50 and 570 ms post bounce. The results of the s9 simulations are shown in the bottom row, calculated from the GWs emitted between 50 and 420 ms post bounce. The right column shows results from simulations with the RbR+ scheme. The left column shows the results from simulations with the FMD scheme. Blue lines represent the best-resolved models (s20-FMD-H, s20-RbR-H, s9-FMD-H, and s9-RbR-H) and the orange represent lines the low-resolution models (s20-FMD-L, s20-RbR-L, s9-FMD-L, and s9-RbR-L).

in Fig. 9. In Eq. (17), t_0 and t_1 represent the start and the end, respectively, of the time window over which the turbulent energy spectrum is averaged. The top panel of Fig. 9 shows the turbulent energy spectrum averaged over the same time window used to produce the spectral energy density plots of Fig. 6 (50 to 420 ms post bounce for the s9 models and 50 to 570 ms post bounce for the s20 models), and the bottom panel of Fig. 9 represents the average turbulent energy spectrum between 50 and 200 ms post bounce.

For the s20 models, the large peaks at $\ell = 2$ seen in the bottom panel of Fig. 9 indicate that a quadrupolar SASI mode (Blondin & Mezzacappa 2006) is superimposed on the convective flow of these models during the first $\sim$ 200 ms of their postbounce evolution. In models s20-FMD-H and s20-RbR-H, the high accretion at early

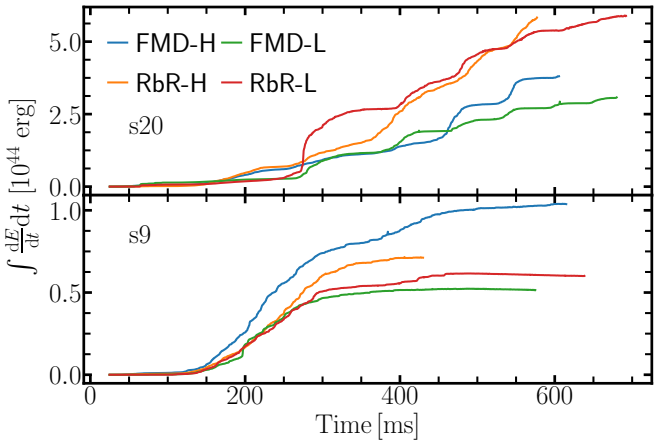

Figure 7. Total time-integrated energy emitted in GWs (Eq. (7)) as a function of time for all eight models. The top panel shows results for the s20 simulations. The results of the s9 simulations are shown in the bottom panel. The x-axis gives the time after core-bounce. The curves show the emitted energy from the beginning of the simulations until the time indicated on the x-axis.

times combined with the quadrupolar asymmetries induced by the SASI create ideal conditions for strong GW emission between 50 and 200 ms after core bounce. The early-time emission of models s20-FMD-H and s20-RbR-H is similar to, although weaker than, the low-frequency emission seen in model m15fr of Andresen et al. (2019). While the dynamics of m15fr and the s20 models differ substantially, the turbulent energy spectrum of model m15fr peaks at $\ell = 2$ (Summa et al. 2018). Model m15fr of Andresen et al. (2019) provides an example of a model where SASI develops soon after core bounce when the accretion rate is high with a turbulent energy spectrum that peaks at $\ell = 2$, and with strong low-frequency GW emission in a narrow frequency range.

Between 200 and 250 ms post bounce an $\ell = 1$ SASI mode starts to grow in the s20 models, and we start to see the typical dipolar deformation of the shock front around this time. The emergence of a dipolar SASI mode around 250 ms is also evident from the turbulent energy spectrum. Compared to the turbulent energy spectrum of the flow between 50 and 200 ms post bounce, the energy at $\ell = 1$ increases by a factor of 10 when averaging the turbulent energy between 50 and 570 ms post bounce, compare the top and bottom panels of Fig. 9.

In the end, we can not conclusively answer all of the questions raised by the strong low-frequency emission at early times in the s20 models. It seems likely that the SASI is responsible for this emission, but it is difficult to definitively prove the existence of a low-amplitude SASI mode. Furthermore, it is unclear where the differences between the s20-RbR-H and s20-FMD-H come from. The distribution of energy over various scales and the total energy contained in turbulent mass motions in model s20-FMD-H and s20-RbR-H are in good agreement during the first 200 ms after bounce (bottom panel of Fig. 9). There is no evidence to indicate that the differences between s20-FMD-H and s20-RbR-H, before 250 ms post bounce, are due to anything else than stochastic variations in the fluid flow.

Interestingly, the turbulent energy spectra of the s9 models also peak at $\ell = 2$, but the peak is roughly a factor two smaller than the peak in the s20 models. The $\ell = 2$ peak in the turbulent energy spectra may correspond to low-amplitude SASI activity, which never develops into large shock oscillations. The growth of the SASI is disfavored in the s9 models due to their continuous shock expansion and corresponding long advection time scales. However, it is more likely that the spectral peak at $\ell = 2$ is connected to large convective plumes deforming the shock front, because the χ parameter in the s9 models is huge (> 10; Glas et al. (2019)).

5 LOW-RESOLUTION SIMULATIONS

We now turn our attention to the four simulations carried out with an angular and radial grid resolution which was two times coarser than in the high-resolution runs.

5.1 Model Dynamics

Models s9-RbR-L and s9-FMD-L closely resemble their high-resolution counterparts. The PNS properties do not change when reducing the resolution, and the properties of the PNS are identical in all models of the low-resolution set (see Fig. 1). The postshock flow of both models is dominated by neutrino-driven convection that develops around 100 ms post bounce and lasts until the onset of rapid shock expansion around 200 ms later. Between 100 and 275 ms post bounce, the average shock radius is smaller by $\sim 1-10$ km in the low-resolution models than in models s9-RbR-H and s9-FMD-H.

The dynamics of models s20-FMD-L and s20-RbR-L are in good agreement with the high-resolution simulations, but there are some differences in the details of the flow. The shock, both in s20-FMD-L and s20-RbR-L, undergoes the same initial expansion as seen in the high-resolution models, peaking around 100 ms after bounce. During the expansion phase, the average shock radii of all models agree well with each other. Once the shock starts to recede, models s20-FMD-L and s20-RbR-L exhibit lower average shock radii than the corresponding high-resolution simulations. The smaller average shock radii in the low-resolution models foster the SASI and this is reflected in the turbulent energy spectra of the models. Compared to the high-resolution models, more of the turbulent energy is concentrated at $\ell = 1$ in the low-resolution models (see Fig. 9). The increase of energy at $\ell = 1$ is fully compatible with the higher numerical viscosity associated with lowering the resolution. The shock, in both models, reaches a local minimum at around 200 ms post bounce. From this point on, model s20-FMD-L evolves similarly to the high-resolution models. The shock in model s20-FMD-L undergoes periods of expansion and contraction, which are caused by alternating periods of SASI and convection in the postshock layer. The same is true for model s20-RbR-L, but both the average shock radius and its oscillations are on average larger than in the other three simulations. Furthermore, model s20-RbR-L exhibits a phase where the average shock radius is significantly larger than in the other three models. Between 250 and 350 ms after bounce the average shock radius of model s20-RbR-L is $\sim$ 10-30 km larger than the shock radius of models s20-FMD-L, s20-RbR-H, and s20-FMD-H.

5.2 Properties of the Gravitational Waves

In Fig. 10 we show the GW amplitudes of s9-FMD-L and s9-RbR-L, the corresponding spectrograms are shown in Fig. 11. The amplitudes and spectrograms of s20-FMD-L and s20-RbR-L are shown

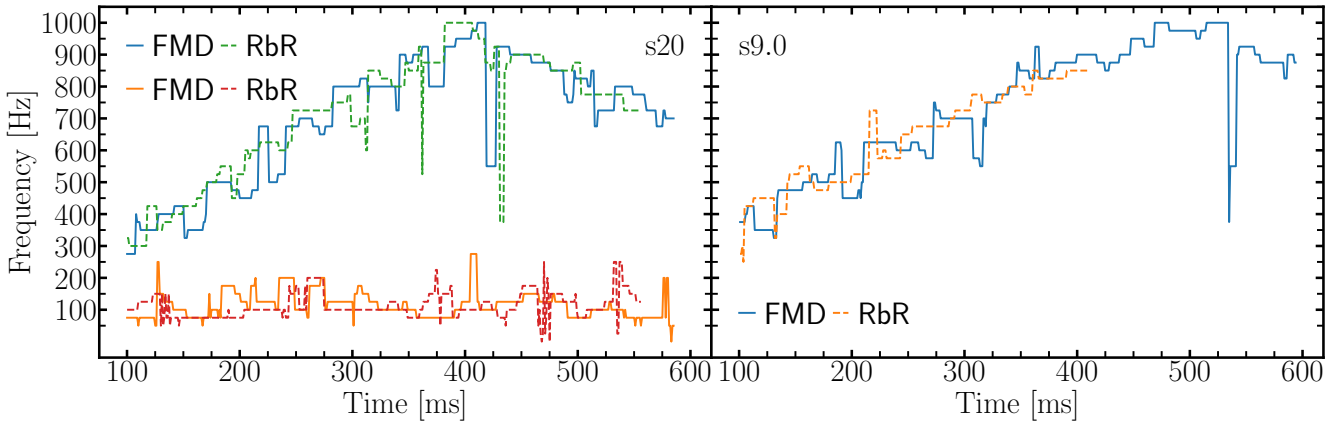

Figure 8. The peak-frequency of the two main signal components as a function of time after core bounce. The left panel represents the models s20-RbR-H and s20-FMD-H. The right panel represents s9-RbR-H and s9-FMD-H. Dashed lines indicate simulations using the RbR+ scheme. Solid lines represent simulations using FMD transport. In the left-hand side panel, we show four lines, the orange and red curves represent the central frequency of the emission below 250 Hz and the blue and green curves represent the peak-frequency of the emission above 250 Hz. In the right panel, we only show two lines, since the s9 models do not have strong low-frequency GW emission. The peak frequencies are extracted from the Fourier analysis of the signals.

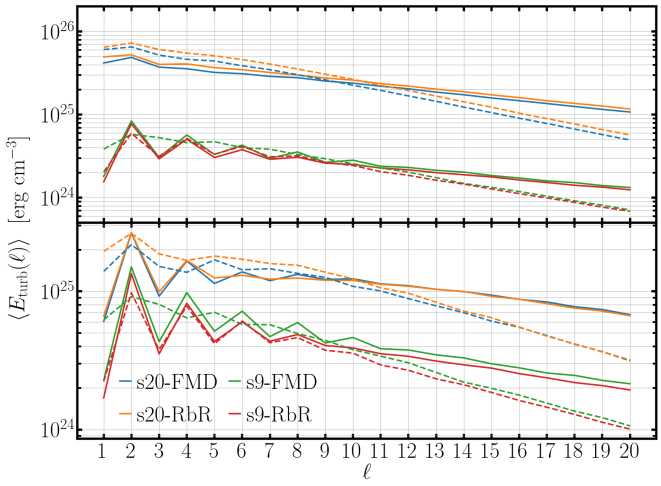

Figure 9. Time averaged turbulent kinetic energy spectrum of the mass motions in the postshock layer, as defined by Eq. (17). The top panel shows results obtained by averaging between 50 and 420 ms post bounce for the s9 models and between 50 to 570 ms post bounce for the s20 models. The bottom panel shows the average turbulent kinetic energy spectrum in the time interval 50 and 200 ms post bounce for all models. Solid lines denote high-resolution models and dashed lines represent the low-resolution models.

in Fig. 12 and Fig. 13, respectively. In the spectrograms, we overplot the curves shown in Fig. 8, which helps us compare the typical characteristics of the signals from the models with high and low resolution. To improve the readability of the plot, we applied a running Hanning window, 25 ms broad, to smooth the curves from Fig. 8.

Glas et al. (2019) found very similar evolution for all four simulations based on the less massive progenitor. The average shock radius, the neutrino emission, and the properties of the PNS show a high degree of similarity in every realisation of the post-bounce evolution of the s9 progenitor. Consequently, the GW signals are also very similar. As in the case of the high-resolution simulations, the average properties of the emission from models s9-FMD-L and s9-RbR-L are virtually indistinguishable. We can see from Fig. 6 that the emission in the low-resolution simulations of s9 is weaker than in the high-resolution runs.

The emission of models s20-FMD-L and s20-RbR-L is similar to their better-resolved counterparts, but the high-frequency emission almost vanishes during four distinct periods and is significantly reduced during two periods in model s20-FMD-L. The four periods of no emission occur at approximately 200, 350, 425, and 575 ms post bounce. The first epoch of reduced emission starts roughly 500 ms after bounce and the second at 625 ms post bounce. The signals from model s20-RbR-L only show one time period, around 375 ms post bounce, where the high-frequency emission completely vanishes. Additionally, the RbR+ model undergoes three periods of reduced high-frequency emission, at approximately 200, 525 and 600 ms post bounce. However, the reduction of the intensity in the spectrograms is an order of magnitude weaker compared to what we see during equivalent episodes in model s20-FMD-L. As it was the case for the high-resolution models, this emission at low-frequencies is intermittent because of the alternating periods of SASI and convection in the postshock layer. The early-time (prior to 250 ms post bounce) emission we saw in the models s20-FMD-H and s20-RbR-H is also present in the low-resolution models.

5.3 Differences induced by decreasing the resolution

The peak-frequencies of the GW emission are not drastically affected by changing the resolution. The overlap of the black curves, which represent the peak-frequencies of the emission from the corresponding high-resolution simulations, with emission regions in Fig. 11 and Fig. 13 demonstrates that the spectral properties of the high- and low-resolution models are in good qualitative agreement. Glas et al. (2019) did not find significant changes in the PNS properties between models with different resolution. The shock trajectory of the high-resolution and low-resolution models show some variability, but the differences in the average shock are only $\sim$ 10 per cent. These differences are significant in terms of the model dynamics, but not large enough to have a drastic impact on the typical frequency of the GW emission.

On the other hand, the periods during which the high-

frequency signal almost entirely subsides in model s20-FMD-L point to substantial resolution-dependent differences in the GW signals from the s20 models. The quiescent periods around 400 and 475 ms post bounce in model s20-FMD-L can be identified in model s20-FMD-H, too, but the reduction in the GW emission is not as strong. This is particularly true for the episode starting at 400 ms post bounce. The phases of weak or suppressed high-frequency emission that we see in the s20 models are correlated with periods of shock expansion. Downflows to the PNS become weaker during phases of shock expansion and thus trigger less high-frequency GW emission from the PNS surface layers. This suppression of high-frequency emission is weaker in the high-resolution models and less prominent in the RbR+ simulations. This is likely due to the stronger convective activity in models with either higher resolution, which have less numerical viscosity, or with RbR+ transport, where local hot spots of neutrino heating are stronger drivers of convection in phases when the shock expands. Both RbR+ and higher resolution therefore facilitate a more continuous emission of high-frequency GWs.

Melson et al. (2020) found that the higher numerical viscosity in low-resolution simulations suppressed the growth of convective activity. When the shock front contracts and neutrino-driven convection is already disfavored, the increased numerical viscosity can push the models into a regime where neutrino-driven convection is significantly reduced in strength [1]. This is reflected in the so-called χ-parameter. Foglizzo et al. (2006) showed that, if the growth of the perturbations is linear, convection in the postshock layer is disfavored when the χ-parameter is less than three. Comparing the second to last panel in Fig. 6 of Glas et al. (2019) to Fig. 13, we see a clear correlation between low χ values and quiescent phases in the GW emission above 300 Hz. In model s20-FMD-L the χ-parameter (see Fig. 6 of Glas et al. (2019)) shows prominent minima at approximately 200 ms and 350 ms post bounce. Both instances are associated with reduced high-frequency GW emission, with the latter correlating to a period of no high-frequency radiation. The systematically larger average shock radius, which is typically ∼ 5-10 km larger in model s20-RbR-L than in s20-FMD-L, in combination with large local variations in the neutrino-heating rate is most likely responsible for keeping convection active in the RbR+ model during periods where emission subsides in model s20-FMD-L. The conclusion that the RbR+ scheme is at least partly responsible for reducing the prominence of the quiescent phases is supported by the fact that periods of weak emission are more pronounced in model s20-FMD-H than in model s20-RbR-H since the shock trajectories of these two models are very similar.

It is interesting to note that the absence of all but one quiescent phase at 350 ms after bounce in model s20-RbR-L means that its emission more closely resembles the signals from models s20-FMD-H and s20-RbR-H than s20-FMD-L.

The large average shock radius between 250 and 350 ms post bounce in model s20-RbR-L lowers the typical frequency associated with the SASI. On the other hand, it is important to note that the emission is typically spread out in a frequency band of approximately 100 Hz and it is, therefore, difficult to disentangle short-term shifts in the central frequency of the emission from inherent stochastic variation.

[1] Note that we find the same resolution dependence of the turbulent energy spectra as Melson et al. (2020). Compared to the high-resolution models, the low-resolution models show a reduction of kinetic energy at small scales ($\ell \geqslant 10$) and an increase of energy at scales below $\ell = 10$. We refer the reader to Melson et al. (2020) for a detailed discussion about how resolution affects the turbulent energy spectra and the total kinetic energy in the postshock layer. In short lowering the resolution decreases the efficiency at which energy deposited by neutrinos is converted into non-radial kinetic energy.

6 SUMMARY AND CONCLUSION

The main goal of this work was to study the theoretical GW emission from 3D core-collapse supernova simulations with two different neutrino transport schemes, the RbR+ method and the FMD transport scheme, to determine if the approximations of the RbR+ method is detrimental for making useful GW signal predictions, see Skinner et al. (2016); Just et al. (2018) and Glas et al. (2019) for discussions about the potential problems of the RbR+ method. We studied a set of eight models, based on two progenitors. For each progenitor, the post-bounce evolution was simulated with the two different neutrino transport methods and at two different resolutions (Glas et al. 2019). Consequently, we studied the impact of numerical resolution and neutrino transport on the GW emission. Our main findings can be summarised as follows:

(i) Differences between the RbR+ and FMD models are, overall, relatively minor for the best-resolved models. The spectrograms (Figs. 3 and 5) display the same basic features. Low-frequency GW emission (below ∼250-300 Hz) is connected to SASI activity. Model s20-RbR-H, and to a lesser degree model s20-FMD-H, show strong low-frequency emission before 200 ms post bounce. The strong emission is most likely due to a qudrapolar SASI mode which is superimposed on the convective flow during the first 200 ms post bounce in the s20 models. High-frequency emission originates from g-modes in the layers near the surface of the PNS and is mainly driven by accretion downflows. The characteristic frequencies of the low- and high-frequency emission agree well between all models (Fig. 8).

(ii) For the s20 models, the RbR+ simulations are more energetic than the FMD simulations and the RbR+ simulations emit more GWs at frequencies between the two main signal components (Figs. 5, 13, and 6). For the s9 models, s9-FMD-H is more energetic than s9-RbR-H (Fig. 7). Models s9-FMD-L and s9-RbR-L are similar both in terms of their spectral energy density and the total emitted energy, with the RbR+ model being slightly more energetic (Fig. 7).

(iii) Lower resolution, associated with higher numerical viscosity, damps convective mass motions in the postshock layer and, consequently, g-mode activity in the PNS surface layer. In s20-FMD-L this leads to the appearance of quasi-periodic intermittent phases of GW emission.

(iv) The periodic suppression of emission is much weaker in the high-resolution models, due to the lower numerical viscosity. It is also weaker in the RbR+ models, where stronger local variations of the neutrino-heating rate provide additional forcing to postshock convection.

The main signal features of the GWs from the RbR+ and FMD models are in very good agreement with each other and it is hard to distinguish between signals from simulations using different neutrino transport schemes. The amplitude and typical emission frequencies of the two main signal components agree well in all models. The excellent agreement is due to the fact that the PNS mass and radius, average shock radius, and preshock mass accretion rate are almost independent of the neutrino transport method. The average shock radius differs the most between different models, but the

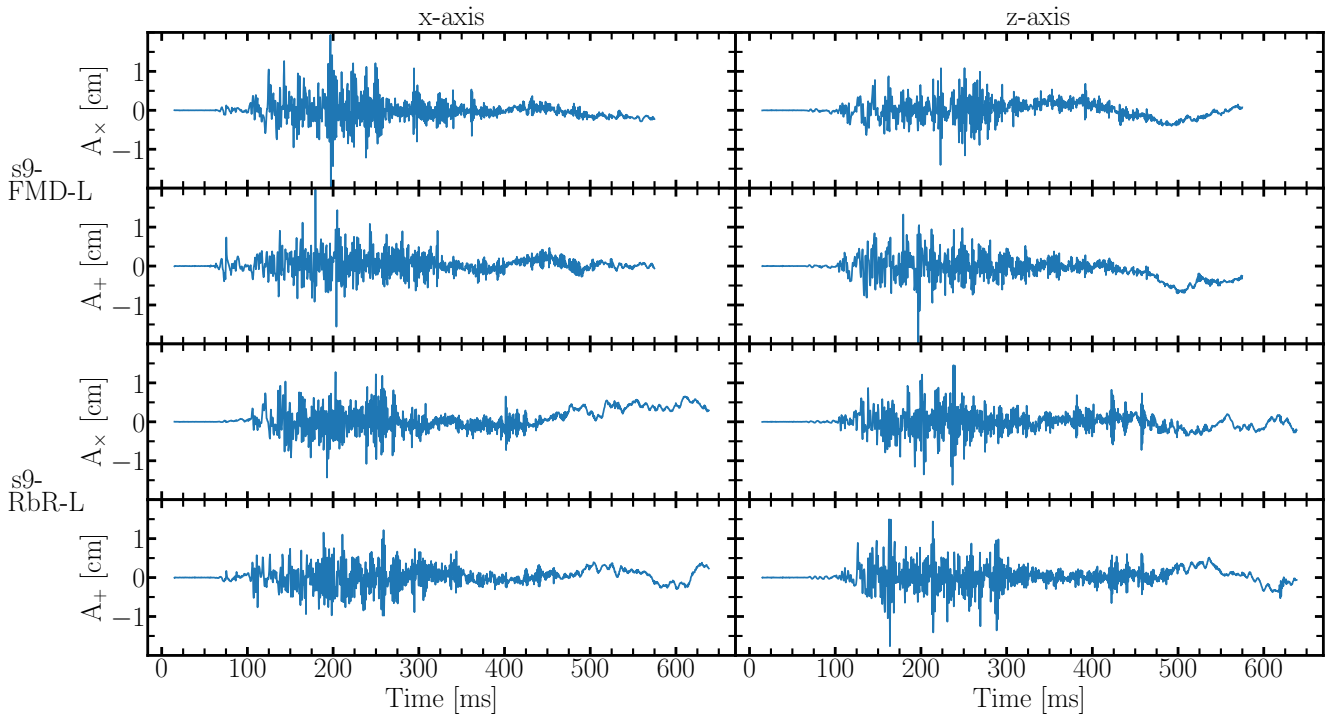

Figure 10. GW amplitudes A_+ and $A_\times$ as functions of time after core bounce for models s9-FMD-L (top two rows) and s9-RbR-L (bottom two rows). The two columns show the amplitudes for two observers, one along the z-axis (right) and one along the x-axis (left).

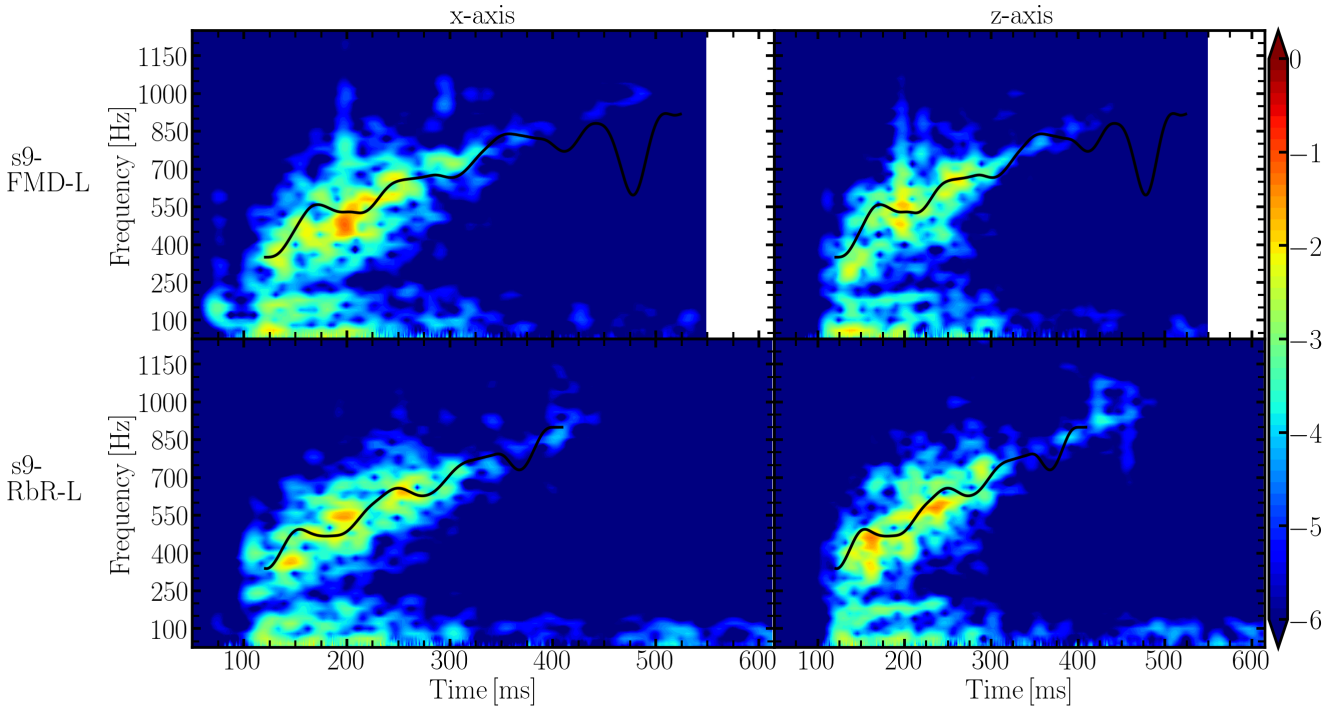

Figure 11. Spectrograms, as defined by Eq. (5), for models s9-FMD-L (top) and s9-RbR-L (bottom). Time is given in ms after core bounce. The two columns represent two observers, one situated along the z-axis (right) and one along the x-axis (left). The black curves are smoothed versions of the curves shown in the right panel of Fig. 8. The colour scale is logarithmic.

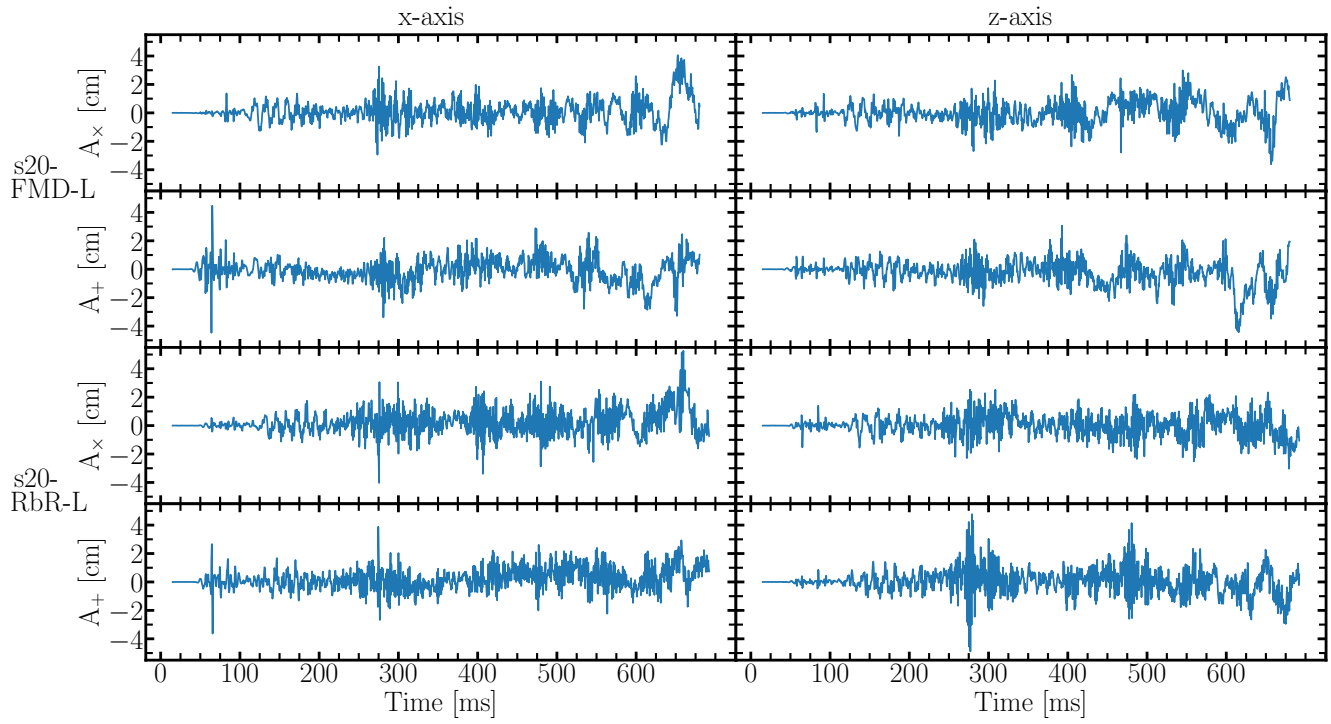

Figure 12. GW amplitudes A_+ and $A_\times$ as functions of time after core bounce for models s20-FMD-L (top two rows) and s20-RbR-L (bottom two rows). The two columns show the amplitudes for two observers, one along the z-axis (right) and one along the x-axis (left).

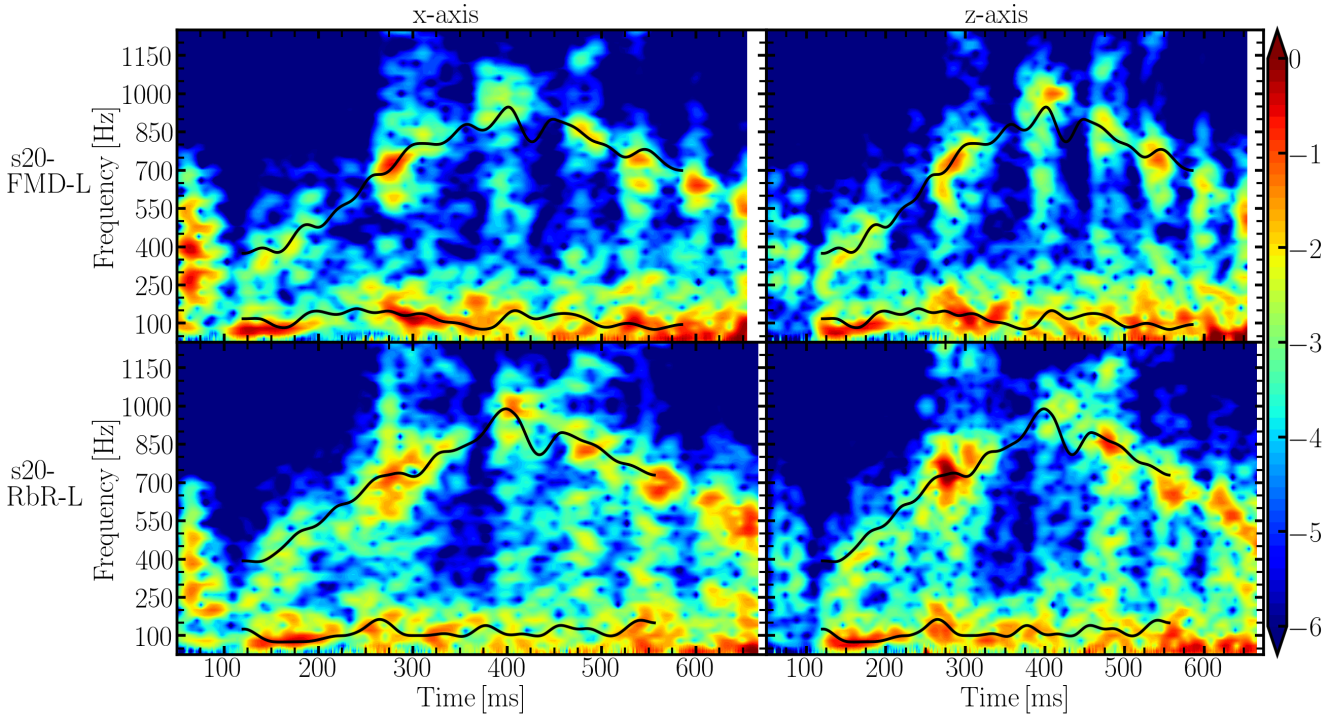

Figure 13. Spectrograms, as defined by Eq. (5), for models s20-FMD-L (top) and s20-RbR-L (bottom). Time is given in ms after core bounce. The two columns show the amplitudes for two observers, one along the z-axis (right) and one along the x-axis (left). The black curves are smoothed versions of the curves shown in the left panel of Fig. 8. The colour scale is logarithmic.

differences are not large enough to cause any significant shift in the spectral properties of the GW emission. There are differences in the fine structure of the GW signals, which might be partly stochastic and could also, to a lesser degree, be linked to the stronger local variations of the neutrino heating in the RbR models.

We did not find any systematic trends as a function of neutrino transport scheme. For example, based on the s20 simulations one would conclude that the RbR+ simulations were more energetic than the FMD simulations, but this was not the case for the s9 simulations. A more extensive model set is necessary to uncover systematic differences in the GW emission from FMD and RbR+ simulations. Furthermore, the artefacts of the RbR+ simulations decrease with higher resolution, because the finer spacing of the computational grid causes the local variations in the RbR+ models to shrink spatially. Overall, changing the resolution has a more significant impact on the model evolution and differences in the GWs than changing the transport scheme.

The small differences that we *tentatively* concluded to be associated with the RbR+ transport, for example enhanced driving of postshock instabilities by larger variations in the local neutrino-heating rate compared to FMD models, are likely to become irrelevant once pre-collapse perturbations in the convectively active burning layers of the progenitor star are included. In this respect, our study was idealised because the hydrodynamic instabilities were seeded by small random perturbations (on the level of 0.1% of the density in the infall region). These small perturbations in the matter falling through the stalled shock wave were dominated by the RbR+ heating variations in the postshock layer, whereas with realistic progenitor perturbations this situation would be reversed.

The signals from core-collapse simulations are inherently stochastic and noisy; relatively large differences can be seen in predictions made by different groups. If we aimed to build a catalogue to be used in matched-filtered searches for laser interferometers, then the differences between the signals presented in this work would be unacceptable. However, the numerical complexity and physical uncertainties of the core-collapse problem make such efforts impossible. A more realistic goal is to produce GW signals that reasonably well predict the essence of emission from core-collapse supernovae, but with the understanding that the exact details can not be accurately predicted. The excellent agreement of the central frequencies (Fig. 8) and typical amplitudes (Fig. 2 and Fig. 2) leads us to the conclusion that using the RbR+ approximation is not detrimental to the prediction of core-collapse supernova GWs.

Finally a note on aliasing. Unfortunately, the sampling rate of our signals was the same as in Andresen et al. (2017) and Andresen et al. (2019). This means that we have a Nyquist frequency of 1000 Hz. Once the Brunt-Väisäla frequency surpasses this value we lose confidence in the accuracy of the signals. Radice et al. (2019) found that PNS oscillations were the most robust source of GW emission in their models. Andresen et al. (2017) and Andresen et al. (2019) concluded that the SASI leads to strong GW emission, whereas Radice et al. (2019) hypothesize that this conclusion is, at least partly, due to aliasing. It is not clear that the connection can made so readily. The strength of the SASI generated emission depends strongly on the vigour of the SASI oscillations, the properties of the flow during the SASI period, and the SASI mode. If strong SASI does not develop, which is the case for all but one of the models presented by Radice et al. (2019), then naturally the associated GW signal will not dominate the emission. Ultimately this is a discussion about the development and nature of the SASI, not one of aliasing.

7 ACKNOWLEDGEMENTS

This work was supported by Deutsche Forschungsgemeinschaft (DFG, German Research Foundation) through Sonderforschungsbereich (Collaborative Research Centre) SFB-1258 “Neutrinos and Dark Matter in Astro- and Particle Physics (NDM)” and under Germany’s Excellence Strategy through Cluster of Excellence ORIGINS (EXC-2094)—390783311 and by the European Research Council through ERC-AdG No. 341157-COCO2CASA. Computer resources for this project have been provided by the Leibniz Supercomputing Centre (LRZ) under grant pr62za, and by the Max Planck Computing and Data Facility (MPCDF) on the HPC system Hydra.

References

Abbott B. P., et al., 2016, Phys. Rev. D, 94, 102001
Abbott B. P., et al., 2020, Phys. Rev. D, 101, 084002
Andresen H., Müller B., Müller E., Janka H.-T., 2017, MNRAS, 468, 2032
Andresen H., Müller E., Janka H. T., Summa A., Gill K., Zanolin M., 2019, Monthly Notices of the Royal Astronomical Society, 486, 2238
Astone P., Cerdá-Durán P., Di Palma I., Drago M., Muciaccia F., Palomba C., Ricci F., 2018, Phys. Rev. D, 98, 122002
Blanchet L., Damour T., Schäfer G., 1990, MNRAS, 242, 289
Blondin J. M., Mezzacappa A., 2006, ApJ, 642, 401
Blondin J. M., Mezzacappa A., DeMarino C., 2003, ApJ, 584, 971
Bruenn S. W., et al., 2013, ApJ, 767, L6
Buras R., Janka H.-T., Rampp M., Kifonidis K., 2006, A&A, 457, 281
Finn L. S., 1989, in Evans C. R., Finn L. S., Hobill D. W., eds, Frontiers in Numerical Relativity. Cambridge University Press, Cambridge (UK), pp 126–145
Foglizzo T., Scheck L., Janka H.-T., 2006, ApJ, 652, 1436
Foglizzo T., Galletti P., Scheck L., Janka H.-T., 2007, ApJ, 654, 1006
Foglizzo T., et al., 2015, Publ. Astron. Soc. Australia, 32, 9
Gill K., Wang W., Valdez O., Szczepanczyk M., Zanolin M., Mukherjee S., 2018, arXiv e-prints, p. arXiv:1802.07255
Glas R., Just O., Janka H. T., Obergaulinger M., 2019, ApJ, 873, 45
Gossan S. E., Sutton P., Stuver A., Zanolin M., Gill K., Ott C. D., 2016, Phys. Rev. D, 93, 042002
Guilet J., Foglizzo T., 2012, MNRAS, 421, 546
Hanke F., Müller B., Wongwathanarat A., Marek A., Janka H.-T., 2013, ApJ, 770, 66
Janka H.-T., 2017, Neutrino-Driven Explosions. Springer International Publishing, Cham, pp 1095–1150, doi:10.1007/978-3-319-21846-5_109, https://doi.org/10.1007/978-3-319-21846-5_109
Just O., Obergaulinger M., Janka H. T., 2015, MNRAS, 453, 3386
Just O., Bollig R., Janka H. T., Obergaulinger M., Glas R., Nagataki S., 2018, MNRAS, 481, 4786
Kuroda T., Takiwaki T., Kotake K., 2016a, ApJS, 222, 20
Kuroda T., Kotake K., Takiwaki T., 2016b, ApJ, 829, L14
Kuroda T., Kotake K., Hayama K., Takiwaki T., 2017, ApJ, 851, 62
Lentz E. J., et al., 2015, ApJ, 807, L31
Logue J., Ott C. D., Heng I. S., Kalmus P., Scargill J. H. C., 2012, Phys. Rev. D, 86, 044023
Marek A., Dimmelmeier H., Janka H.-T., Müller E., Buras R., 2006, A&A, 445, 273
Marek A., Janka H., Müller E., 2009, A&A, 496, 475
Melson T., Janka H.-T., Marek A., 2015, ApJ, 801, L24
Melson T., Kresse D., Janka H.-T., 2020, ApJ, 891, 27
Mezzacappa A., et al., 2020, Phys. Rev. D, 102, 023027
Morozova V., Radice D., Burrows A., Vartanyan D., 2018, ApJ, 861, 10
Müller B., 2015, MNRAS, 453, 287
Müller B., Janka H.-T., 2014, ApJ, 788, 82
Müller E., Janka H.-T., Wongwathanarat A., 2012, A&A, 537, A63
Müller B., Janka H.-T., Marek A., 2013, ApJ, 766, 43
Müller B., Melson T., Heger A., Janka H.-T., 2017, MNRAS, 472, 491

Murphy J. W., Ott C. D., Burrows A., 2009, ApJ, 707, 1173
O'Connor E. P., Couch S. M., 2018, The Astrophysical Journal, 865, 81
Obergaulinger M., 2008, Dissertation, Technische Universität München, München
Ohnishi N., Kotake K., Yamada S., 2006, ApJ, 641, 1018
Ohnishi N., Iwakami W., Kotake K., Yamada S., Fujioka S., Takabe H., 2008, Journal of Physics Conference Series, 112, 042018
Oohara K.-i., Nakamura T., Shibata M., 1997, Progress of Theoretical Physics Supplement, 128, 183
Ott C. D., Roberts L. F., da Silva Schneider A., Fedrow J. M., Haas R., Schnetter E., 2018, ApJ, 855, L3
Powell J., 2018, Classical and Quantum Gravity, 35, 155017
Powell J., Müller B., 2019, MNRAS, 487, 1178
Powell J., Müller B., 2020, MNRAS,
Powell J., Gossan S. E., Logue J., Heng I. S., 2016, Phys. Rev. D, 94, 123012
Powell J., Szczepanczyk M., Heng I. S., 2017, Phys. Rev. D, 96, 123013
Radice D., Morozova V., Burrows A., Vartanyan D., Nagakura H., 2019, ApJ, 876, L9
Rampp M., Janka H.-T., 2002, A&A, 396, 361
Roberts L. F., Ott C. D., Haas R., O'Connor E. P., Diener P., Schnetter E., 2016, ApJ, 831, 98
Roma V., Powell J., Heng I. S., Frey R., 2019, Phys. Rev. D, 99, 063018
Scheck L., Janka H.-T., Foglizzo T., Kifonidis K., 2008, A&A, 477, 931
Skinner M. A., Burrows A., Dolence J. C., 2016, ApJ, 831, 81
Sotani H., Takiwaki T., 2020, arXiv e-prints, p. arXiv:2004.09871
Sotani H., Kuroda T., Takiwaki T., Kotake K., 2017, Phys. Rev. D, 96, 063005
Steiner A. W., Hempel M., Fischer T., 2013, ApJ, 774, 17
Sukhbold T., Ertl T., Woosley S. E., Brown J. M., Janka H. T., 2016, ApJ, 821, 38
Summa A., Janka H.-T., Melson T., Marek A., 2018, ApJ, 852, 28
Suvorova S., Powell J., Melatos A., 2019, Phys. Rev. D, 99, 123012
Takiwaki T., Kotake K., Suwa Y., 2012, ApJ, 749, 98
Takiwaki T., Kotake K., Suwa Y., 2014, ApJ, 786, 83
Torres-Forné A., Cerdá-Durán P., Passamonti A., Font J. A., 2018, MNRAS, 474, 5272
Torres-Forné A., Cerdá-Durán P., Obergaulinger M., Müller B., Font J. A., 2019a, Phys. Rev. Lett., 123, 051102
Torres-Forné A., Cerdá-Durán P., Passamonti A., Obergaulinger M., Font J. A., 2019b, MNRAS, 482, 3967
Vartanyan D., Burrows A., Radice D., 2019, MNRAS, 489, 2227
Wongwathanarat A., Janka H., Müller E., 2010, ApJ, 725, L106
Wongwathanarat A., Müller E., Janka H.-T., 2015, A&A, 577, A48
Woosley S. E., Heger A., 2007, Phys. Rep., 442, 269
Woosley S. E., Heger A., 2015, ApJ, 810, 34
Yakunin K. N., et al., 2015, Phys. Rev. D, 92, 084040
van Putten M. H. P. M., 2016, ApJ, 819, 169